10-5-2015

Sun-Like Magnetic Cycles in the Rapidly Rotating Young Solar Analog HD 30495

Ricky Egeland
National Center for Atmospheric Research

Travis S. Metcalfe
Space Science Institute

Jeffrey C. Hall
Lowell Observatory

Gregory W. Henry
Tennessee State University

Recommended Citation

Ricky Egeland et al 2015 ApJ 812 12

The Astrophysical Journal, 812:12 (11pp), 2015 October 10 doi:10.1088/0004-637X/812/1/12

SUN-LIKE MAGNETIC CYCLES IN THE RAPIDLY ROTATING YOUNG SOLAR ANALOG HD 30495

Ricky Egeland[1,2], Travis S. Metcalfe[3,4], Jeffrey C. Hall[5], and Gregory W. Henry[6]
[1] High Altitude Observatory, National Center for Atmospheric Research, P.O. Box 3000, Boulder, CO 80307-3000, USA; egeland@ucar.edu
[2] Department of Physics, Montana State University, Bozeman, MT 59717-3840, USA
[3] Space Science Institute, 4750 Walnut St. Suite 205, Boulder, CO 80301, USA
[4] Stellar Astrophysics Centre, Department of Physics and Astronomy, Aarhus University, Ny Munkegade 120, DK-8000 Aarhus C, Denmark
[5] Lowell Observatory, 1400 West Mars Hill Road, Flagstaff, AZ 86001, USA
[6] Center of Excellence in Information Systems, Tennessee State University, 3500 John A. Merritt Blvd., Box 9501, Nashville, TN 37209, USA
Received 2015 April 15; accepted 2015 August 18; published 2015 October 5

ABSTRACT

A growing body of evidence suggests that multiple dynamo mechanisms can drive magnetic variability on different timescales, not only in the Sun but also in other stars. Many solar activity proxies exhibit a quasi-biennial (∼2 year) variation, which is superimposed upon the dominant 11 year cycle. A well-characterized stellar sample suggests at least two different relationships between rotation period and cycle period, with some stars exhibiting long and short cycles simultaneously. Within this sample, the solar cycle periods are typical of a more rapidly rotating star, implying that the Sun might be in a transitional state or that it has an unusual evolutionary history. In this work, we present new and archival observations of dual magnetic cycles in the young solar analog HD 30495, a ∼1 Gyr old G1.5 V star with a rotation period near 11 days. This star falls squarely on the relationships established by the broader stellar sample, with short-period variations at ∼1.7 years and a long cycle of ∼12 years. We measure three individual long-period cycles and find durations ranging from 9.6 to 15.5 years. We find the short-term variability to be intermittent, but present throughout the majority of the time series, though its occurrence and amplitude are uncorrelated with the longer cycle. These essentially solar-like variations occur in a Sun-like star with more rapid rotation, though surface differential rotation measurements leave open the possibility of a solar equivalence.

Key words: dynamo – stars: activity – stars: individual (HD 30495) – stars: rotation – stars: solar-type

Supporting material: machine-readable tables

1. BACKGROUND AND CHARACTERIZATION

Stellar magnetic activity cycles have been known in the Sun since Schwabe and were shown to exist in other stars by Wilson (1978) using an activity index derived from flux measurements in the Ca II HK line cores performed at the Mount Wilson Observatory (MWO). The Mount Wilson survey from 1966 to 2003 remains the largest and longest campaign investigating stellar activity, culminating with Baliunas et al. (1995) reporting on the variability of 111 stars, 52 of which were found to demonstrate periodic behavior in a manner similar to our Sun. This periodic behavior is believed to be caused by a magnetic dynamo driven by rotational motions of plasma in the stellar interior. Using the Mount Wilson data along with measurements of surface rotation, Saar & Baliunas (1992) and Soon et al. (1993) first reported two distinct branches of cycling stars, the "active" and "inactive" branches distinguished by their mean activity level and number of rotations per cycle, and furthermore found some stars with multiple prominent periodicities fit on both branches. Observing a subset of high-quality cycle detections from the stellar sample of Saar & Brandenburg (1999), Böhm-Vitense (2007) hypothesized that these classes are due to separate dynamo mechanisms identifiable by their interior shear layer, with the slow-rotating "inactive" branch operating near the base of the convective envelope, and the fast-rotating "active" branch working in rotational shear layers closer to the surface. Curiously, the Sun and its 11 year cycle appear to be a unique outlier in this small stellar sample, falling between the two activity branches. Böhm-Vitense (2007) suggested that the Sun could be in transition from one dominant dynamo mechanism to another.

In addition to the 11 year solar cycle, short-term quasi-periodic variability has been observed in a number of solar phenomena. Various manifestations of the so-called quasi-biennial oscillation (QBO) of 0.6–4 years are reviewed in Bazilevskaya et al. (2014) and McIntosh et al. (2015). QBOs are found in records of sunspot number and area, magnetic field measurements, solar irradiance, and in magnetically sensitive phenomena such as filaments in H-alpha and variations of field-sensitive lines such as Ca II and Mn I. The QBO also appears in eruptive phenomena—flares, coronal mass ejections, and solar energetic particle events—which arise from magnetically active regions. Short period variations have also been observed in the stars: Baliunas et al. (1995) reported nine stars with significant "secondary cycles." Six of these (and one new addition) were part of the high-quality activity cycles of the Saar & Brandenburg (1999) sample, with the secondary cycle falling on the "inactive" branch. Oláh et al. (2009) performed a time-frequency analysis of multi-decadal photometry and Ca II emission for 20 stars and found 15 of them to exhibit multiple cycles. High-cadence SMARTS HK observations have found short-period variations (1.6 year) on ι Horologi (Metcalfe et al. 2010) and ϵ Eridani (2.95 year), another dual-cycle star with a long-term cycle of 12.7 year (Metcalfe et al. 2013). Fares et al. (2009) used Zeeman Doppler Imaging to observe a polarity-flipping cycle of ∼2 years in the fast-rotating F6 star τ Bootis, which had weak indications of a long-period activity cycle of 11.6 year in Baliunas et al. (1995). This short-period cycle is distinct from the solar QBO phenomena, which does not reverse magnetic polarity.

The origin of the solar QBO and its relation to the solar cycle is not understood. The discovery of periodic variations of 1.3 years in the differential rotation of the deep interior revealed

Table 1
HD 30495 Properties

Property	Value	Reference
Spectral type	G1.5 V	(1)
V	5.49 ± 0.01	(2)
$B - V$	0.632 ± 0.006	(2)
Parallax	75.32 ± 0.36 mas	(2)
$v \sin i$	4.1 ± 0.8 km s^{-1}	(3)
$T_{\rm eff}$	5826 ± 48 K	(4)
$\log g$	4.54 ± 0.012 dex	(4)
[Fe/H]	$+0.005 \pm 0.029$ solar	(4)
Mass	$1.02 \pm 0.01\ M_{\odot}$	(4)
Radius	$0.898 \pm 0.013\ R_{\odot}$	(4*)
Luminosity	$0.837 \pm 0.037\ L_{\odot}$	(4*)
Age	970 ± 120 Myr	(5*)
$\overline{P}_{\rm rot}$	11.36 ± 0.17 days	⋯
ΔP	0.59 ± 0.05 days	⋯
$\Delta\Omega$	$\gtrsim 1.67 \pm 0.15$ deg/day	⋯
$\sin i$	1.0 ± 0.2	⋯
i	$\gtrsim 55\overset{\circ}{.}4$	⋯
$P_{\rm cyc,long}$	$12.2 \pm$ [3.0] year	⋯
$A_{\rm cyc,long}$	$0.118 \pm$ [0.044]	⋯
$P_{\rm short}$	$1.67 \pm$ [0.35] year	⋯
$A_{\rm short}$	$0.066 \pm$ [0.028]	⋯

References. (1) Gray et al. (2006), (2) *Hipparcos*, Perryman et al. (1997), van Leeuwen (2007), (3) Gaidos et al. (2000), (4) Baumann et al. (2010), (4*) Derived from Baumann et al. (2010) measurements, (5*) Derived from Barnes (2007) age–rotation relationship. The lower section of the table are measurements found in this work Quantities in brackets represent one half of the observed range of values.

by helioseismology (Howe et al. 2000) suggests that the QBO is sub-surface in origin and may be an additional feature of a deep-interior dynamo process responsible for the 11-year cycle (see Bazilevskaya et al. 2014 and references therein). McIntosh et al. (2015) also points to a deep interior process, inferring that this short-period variability is driven by the interaction of two oppositely signed magnetic activity bands deep in the interior of each hemisphere. Another possibility is the distinct-dynamo scenario described above as an explanation for the two activity branches in the Saar & Brandenburg (1999)/Böhm-Vitense (2007) stellar sample. Fletcher et al. (2010) find a ∼2 year variation in the frequency shift of solar p-mode oscillations, and locate the origin of the variations to be *below* the source of the 11 year signal in the data. They hypothesize that spatially distinct dynamo processes may be responsible for this phenomenon. Chowdhury et al. (2009) suggested a non-dynamo origin for QBOs: an instability caused by Rossby waves interacting with the tachocline.

While stellar observations cannot match the level of detail in which the solar QBO is observed, the varied physical conditions present in other stars may have an impact on the manifestations of these short-period oscillations that sheds additional light on their origins. In this work, we present new observations of variability in HD 30495 (58 Eri), a nearby young solar analog that demonstrates both a long-term activity cycle and a short-period oscillation, which may be analogous to the solar cycle and QBO. The upper section of Table 1 summarizes the measured global properties of HD 30495. Photometry and spectroscopy show the star to be essentially solar-like, leading previous authors to study this star as a potential solar twin (Cayrel de Strobel 1996; Porto de Mello et al. 2014). Gaidos et al. (2000) found rotational modulations in high-cadence Strömgren b and y photometry to determine a rotation period of 11.3 days, roughly 2.3 times faster than the Sun. Due to the process of magnetic braking, older stars have slower rotations, giving the well-known $P_{\rm rot} \propto t^{1/2}$ age–rotation relationship (Skumanich 1972). The faster rotation of HD 30495 thereby implies it is younger than the Sun, and by the age–rotation relationship given in Barnes (2007) we obtain an age of about ∼1 Gyr. Observations of excess infrared flux attributed to a diffuse and distant debris disk of ∼73 Earth-masses leftover from formation (Habing et al. 2001) give further evidence for a young age. Spectroscopic searches of similar "Vega-like" main-sequence objects with excess infrared emission have ruled out the possibility of dense concentrations of gas close to the star (Liseau 1999; Habing et al. 2001). Based on these studies, in the discussions that follow, we shall assume that the disk is not a contributing factor to the observed magnetic signatures.

Baliunas et al. (1995) previously searched for cyclic variability in HD 30495 using the Lomb–Scargle periodogram on the Mount Wilson S time series from 1966 to 1992, but classified it as "Var," defined as "significant variability without pronounced periodicity" and $\langle \sigma_S / S \rangle \gtrsim 2\%$. The mean activity level was found to be high, $\langle S \rangle = 0.297$, as expected for fast rotators (compare to the solar value from the same study $\langle S_{\odot} \rangle = 0.179$). Hall et al. (2007) S-index measurements from the Solar Stellar Spectrograph (SSS) again found stronger-than-solar activity levels, with $\langle S \rangle = 0.309$. Hall et al. (2009) used twelve years of precise Strömgren b and y photometry from the Fairborn Automated Photometric Telescope (APT) program (Henry 1999), finding a photometric variability for HD 30495 roughly six times solar. Furthermore, brightness was shown to decrease with increased chromospheric activity, indicating that variability in the star's brightness is dominated by dark spots, typical of fast rotators in that study.

Naively, and based solely on its similarity to the Sun and faster rotation and, hence, presumably greater differential rotation, we might expect HD 30495 to have a more vigorous dynamo, leading to higher magnetic activity and a shorter activity cycle. As we shall see, the former is borne out by observations, while the latter is not.

2. ACTIVITY ANALYSIS

We analyze a combined 47-year time series of the Mount Wilson S-index shown in Figure 1. This dimensionless index is defined as the ratio of the core emission in the Fraunhofer H and K lines of Ca II with the nearby continuum regions, as measured by the HKP-1 and later HKP-2 photometers at MWO (Wilson 1968; Vaughan et al. 1978). Ca II H & K global-scale emission reversals are a signature of departure from radiative equilibrium, a defining feature of a chromosphere, and must be due to magnetic non-thermal heating mechanisms. Due to the unsurpassed duration and breadth of the Mount Wilson survey, S, a measure on an *instrumental scale*, has become the de facto standard for measuring stellar magnetic activity, and subsequent surveys have calibrated to the Mount Wilson scale. S is dependent on stellar properties such as temperature, surface gravity, and composition, which precludes its use for directly comparing activity levels of a heterogeneous ensemble. As we focus our analysis on a single star, conversion to a corrected quantity (e.g., R'_{HK}; Noyes et al. 1984) is not necessary.

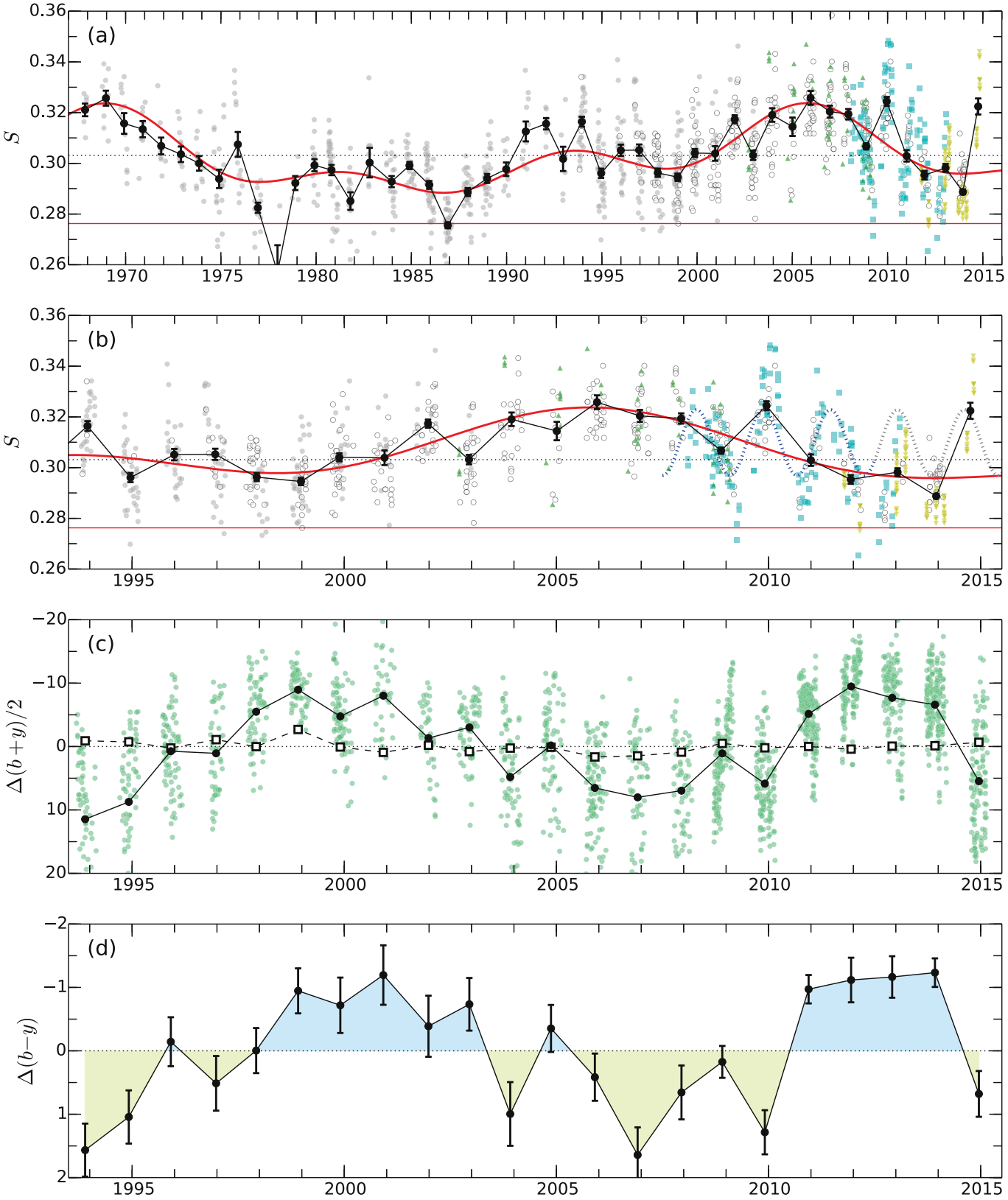

Figure 1. (a) HD 30495 combined *S*-index time series, including data from MWO (•), SSS (○), SMARTS (■), CPS (▲), and HARPS (▼), along with seasonal means (•), with error bars representing the error of the mean. The red curve is a three-component sine wave model of the stellar cycles, while the horizontal red line is our reference point for global activity minimum. (b) Zoomed portion highlighting higher-cadence SMARTS data, with a $P = 1.58$ year sine wave plotted for comparison (blue dashed curve). (c) APT differential photometry brightness measurements in the combined Strömgren *b* and *y* bands, in milli-magnitudes. Differences shown are HD 30495 nightly measurements (•) and seasonal means (•) with respect to the comparison stars, as well as the difference between the two comparison stars (□). (d) Seasonal mean differential brightness difference in the *b* and *y* bands, in milli-magnitudes, with colored regions indicating brighter *b* (blue) and *y* (green) emission. A horizontal dotted line indicates the grand mean in all panels. Magnitude scales are inverted such that brightness increases in the upward direction. The observations shown in this figure are available in the electronic version of this publication. See Tables 3 and 4 in the Appendix.

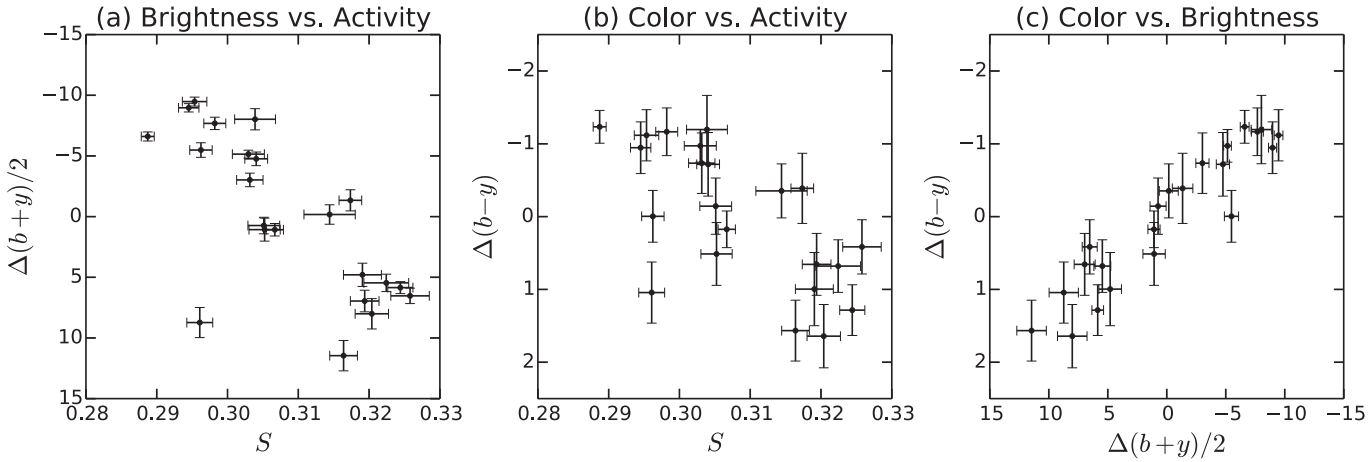

Figure 2. Correlations among seasonal means of activity, brightness, and color from the time series of Figure 1. Error bars indicate the error in the mean. Magnitude scales are in milli-magnitudes and are inverted such that brightness increases in the upward/rightward directions.

The combined S time series in Figure 1(a) contains 1285 measurements from five different instruments. The majority of the measurements (624 measurements from 1967 to 2003) come from the original Mount Wilson survey, calibrated as described in Baliunas et al. (1995). We assumed a uniform measurement error of 3% of the mean for this time series, near the upper limit quoted by Wilson (1968). The next largest portion of the measurements are from the SSS at Lowell Observatory (364 measurements from 1993 to 2014) (Hall & Lockwood 1995), taking the time series from the beginning of the Mount Wilson survey to present day. SSS obtains $R \approx$ 10,000 at Hα spectra, and S is derived by approximating the Ca II H, K and continuum bandpasses used by the MWO instrument. These data are then calibrated to the Mount Wilson instrumental scale using long-duration means of common targets. A typical measurement error of 2.4% was estimated using photon statistics in the K line core and detector properties. Observations from the SMARTS Southern HK survey using the *RC Spec* $R \approx$ 2500 spectrograph at 1.5 m telescope at CTIO are the third largest contribution (140 measurements from 2008 to 2013), and though of shorter duration, this queue-scheduled time series is not plagued by the large seasonal gaps of the other surveys, allowing short-period variation to be better determined. These data were calibrated to the Mount Wilson scale via common observations with SSS targets, as described in Metcalfe et al. (2010). An additional 108 measurements from 2011 to 2015 derived from HARPS $R \approx$ 120,000 spectra from a solar twin planet search (Ramírez et al. 2014; Bedell et al. 2015), again calibrated to the MWO scale using common targets, as described in (Lovis et al. 2011). Finally, we add 49 observations from 2002 to 2008 derived from $R \approx$ 55,000 spectra of the Hamilton Spectrometer at Lick Observatory. These observations[7] are part of the California Planet Search (CPS) and were similarly calibrated to the MWO scale using common targets (Isaacson & Fischer 2010).

Though each of these time series used a global calibration to the Mount Wilson scale using long-term means of commonly observed targets, visual inspection of the combined time series revealed obvious discontinuities and differences in scale. This is likely due to the fact that the *global* calibration involves a compromise linear fit among all targets, while scatter about that fit reveals error in the calibration that would result in a discontinuity in any individual target. We applied a simple calibration that assumes overlapping periods of two different time series ought to agree on the mean for that period. To calibrate S to the scale of S_0, the mean value over the period of overlap, $\overline{S}$ and $\overline{S}_0$ were calculated, and a scaling factor $C = \overline{S}_0/\overline{S}$ was derived. The resulting calibrated time series $S' = CS$ then has an equivalent mean value over the overlapping period to the base series S_0. The resulting scaling factors were $C(\mathrm{SSS} \rightarrow \mathrm{MWO}) = 1.015$, $C(\mathrm{SMARTS} \rightarrow \mathrm{SSS}') = 1.067$, $C(\mathrm{HARPS} \rightarrow \mathrm{SSS}') = 1.074$, $C(\mathrm{CPS} \rightarrow \mathrm{SSS}') = 1.098$. The SMARTS, HARPS, and CPS time series were scaled using overlapping portions of the post-calibration SSS time series, therefore their overall scaling is multiplied by $C(\mathrm{SSS} \rightarrow \mathrm{MWO})$. This calibration removed obvious discontinuities in the combined time series and reduced the standard deviation by 3.8%. The final combined time series has a grand mean $\overline{S} = 0.303$ and a standard deviation $\sigma = 0.0167$. Seasonal means for the combined time series are shown as black circles in Figure 1(a). Following these seasonal means, clear cyclic behavior is visible, emphasized by the cycle model (red curve) described below.

We also examined the 22-year time series of differential photometry acquired with the T4 0.75 m APT at Fairborn Observatory (Henry 1999), shown in Figure 1(c). These measurements, made in the Strömgren b (467 nm) and y (547 nm) bands, are a difference with respect to the mean brightness of two stable comparison stars, HD 31414 and HD 30606. The differential measurements in the b and y bands are then averaged to $(b + y)/2$ to create a "by" band that increases the signal to noise ratio. The unimportant mean difference is subtracted from the time series. The stability of the comparison stars is demonstrated in the seasonal mean of their brightness difference in the by band, shown as white squares in Figure 1(c), with a standard deviation $\sigma = 0.00093$ mag. HD 30495 by brightness is strongly variable ($\sigma = 0.0065$ mag) and out-of-phase with the S-index shown in Figure 1(b). A rank correlation test between S and by seasonal means shows 99.98% significance in the correlation, which is plotted in Figure 2(a). This is interpreted as evidence the star's brightness variations are dominated by dark spots, which are more prevalent during times of activity maximum. Figure 1(d) plots the $\Delta(b - y)$ color index where blue shading indicates negative color index and

[7] http://cdsarc.u-strasbg.fr/viz-bin/Cat?J/ApJ/725/875

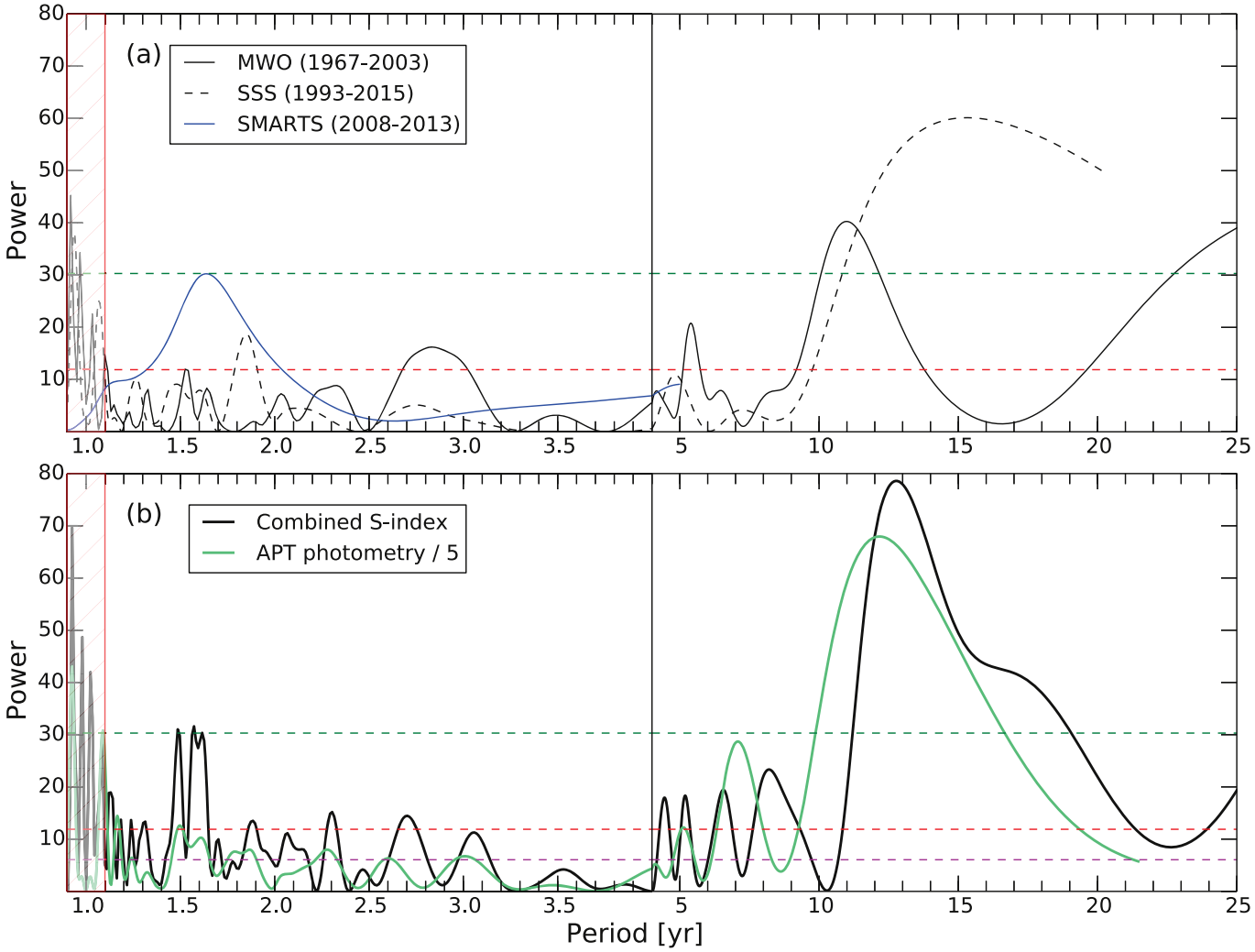

Figure 3. Lomb–Scargle periodograms from the time series of Figure 1. Panel (a) contains the result from single-instrument *S*-index surveys and panel (b) the combined *S*-index time series, as well as the APT photometry of Figure 1(c). Note the division in the period scale. The hatched region near $P \approx 1$ year contains artifacts of the seasonal sampling. The green and red horizontal dashed lines are the "excellent" and "poor" significance thresholds for the *S*-index periodograms, as defined in Baliunas et al. (1995). Note that the APT periodogram is scaled down by a factor of five for easy comparison and the magenta horizontal line is the "excellent" threshold for that series.

green shading indicates positive color index. Comparing panels (b), (c), and (d) of Figure 1, we see that HD 30495 gets bluer as it gets brighter (activity minimum) and redder as it gets fainter (activity maximum). This is shown again more clearly in Figures 2(b) and (c), in particular the remarkably tight color-brightness correlation. We interpret this color shift as an increase in surface temperature during times of activity minima, due to the reduction of cool spots on the surface.

We computed the Lomb–Scargle periodogram (Scargle 1982; Horne & Baliunas 1986) from our time series to find statistically significant periodicities in the data, with the results shown in Figure 3. To verify the robustness of the peaks, we compare the periodogram of the combined time series (thick black line) to those of the individual MWO, SSS, and SMARTS series over shorter intervals, as well as to the periodogram of the $(b + y)/2$ photometry. Not shown in the figure are the large peaks beyond 25 years in the MWO and combined *S*-index periodograms, which are most likely due to the windowing of the entire time series, not true physical variation. The hatched regions of $P < 1.1$ on the left side of periodograms contain a number of large peaks near 1 year, which are aliases due to the seasonal sampling in our time series. We verified these are all aliases by obtaining a least-squares fit of the data to a sine wave with a period set by one of the ∼1 year peaks, then subtracting that signal from the time series and re-computing the periodogram. The new periodogram would no longer contain the ∼1 year peak, and a corresponding low-frequency peak would be removed as well. This established a symmetry between the low-frequency peaks and these ∼1 year peaks, and as a result we do not consider any peak <1.1 years to be physical. (See also Figure 4(c), in which spurious ∼1 year peaks are found in the periodogram of a signal of pure sine waves of lower frequency.)

Following Horne & Baliunas (1986), we calculate the "False Alarm Probability" (FAP) threshold:

$$z = -\ln\left(1 - (1 - F)^{1/N_i}\right) \quad (1)$$

where F is the probability that there exists a peak of height z at any frequency due to random Gaussian noise in the signal, and N_i is the number of independent frequencies in the time series. We computed N_i by generating 5000 random time series with the same sampling times of our data, generating a probability distribution for the maximum peak z, and fitting this distribution

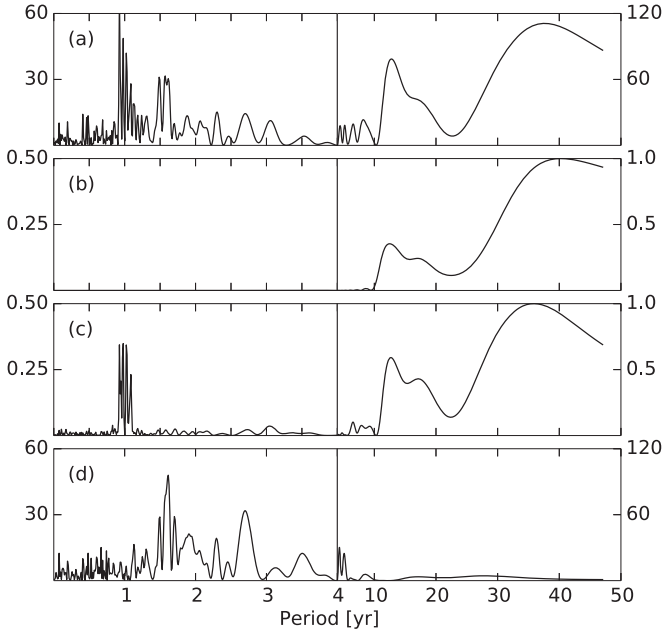

Figure 4. Lomb–Scargle periodogram of (a) the original composite *S*-index time series (b) three-component cycle model with equal-spaced sampling (c) three-component cycle model with the same sampling as the original data (d) the residual of the original data minus the cycle model. Note that period and power scales change at the 4-year mark; the left and right *y*-axis give the power scale for that side. Periodograms of the cycle model are normalized to 1.

to Equation (1) inverted for F, with N_i as the free parameter. The upper threshold (green line) shown in Figure 3 corresponds to $F = 10^{-11}$, the threshold for an "excellent" cycle in Baliunas et al. (1995), and the lower threshold (red line) is for $F = 10^{-3}$ (99.9% significance), the minimum requirement for a "poor" cycle in that work. The FAP thresholds shown are those computed for the combined time series, however they are similar to those obtained for the individual component time series, being only slightly more stringent.

The uncertainties in peak positions were estimated using a Monte Carlo method. In each trial, each time series measurement is randomly sampled from a Gaussian distribution defined by that measurement's value and uncertainty. Then, a periodogram is computed and the new peak position saved. By running 5000 trials, an approximately Gaussian distribution of peak positions is obtained, and the uncertainty is estimated as its standard deviation.

In the combined time series we found four resolved peaks above the "excellent" threshold: a long period peak $P_{\rm long} = 12.77 \pm 0.09$ year, and a cluster of three short-period peaks at $P_{\rm short,1} = 1.572$, $P_{\rm short,2} = 1.486$, and $P_{\rm short,3} = 1.615$ year ($\sigma_{\rm short} \approx 0.003$). The $P_{\rm long}$ peak is found between nearby significant peaks found in the MWO ($P_{\rm long,MWO} = 10.7$ year) and SSS ($P_{\rm long,SSS} = 15.3$ year) time series, and nearby the $P_{\rm long,APT} = 12.2$ peak from *by* photometry. The spread in periods from the earlier MWO data to the later SSS data indicates that, like the Sun, the long-term cycle is only quasi-periodic, and the duration of each individual cycle varies. This increase in period was confirmed in a wavelet analysis of the *S* seasonal means (not shown), which showed the period increasing from ∼10 to ∼14 years over the duration of the time series. The ∼13 year peak in Figure 3(b) has a protruding "shoulder" on its right side, which is due to an unresolved peak near 17 year. This peak was resolved in ∼25% of the Monte Carlo trials done to determine the uncertainty in peak positions, allowing us to measure a mean value of 16.9 year. This ∼17 year period and another large peak at ∼37 year were found to be artifacts of the amplitude structure and/or the duration of the time series (data window). We verified this by computing periodograms of various fractions of the data window (e.g., 2/3 to 1/2 of the total duration) at various offsets and noting that the ∼17 year peak disappears in all cases and the ∼37 year peak shifts close to the duration of the new window.

Figure 3(b) shows the short-period peaks are almost perfectly matched by two peaks (1.49 and 1.61 year) in the APT periodogram. We also find a broad corresponding "excellent"-class peak at 1.63 year in the SMARTS time series and again in the HARPS series at 1.75 year. A less significant "poor"-class peak at 1.85 year is in the SSS data and 1.53 year in the MWO data. The spread in values indicates that these short-period variations are not of a constant frequency, which we investigate in detail in Section 4.

We find that both the long and short-period signals are found consistently in several distinct *S*-index time series of different time intervals, as well as in the APT differential photometry, a measurement using very different observation methods to sample a physically distinct region of the star. This is strong evidence for the co-existence of variability on different time scales and in distinct regions of the stellar atmosphere, analogous to the solar observations of the 11-year cycle and QBO.

3. SIMPLE CYCLE MODEL

In the Sun, each occurrence of rising and falling activity is numbered and, somewhat confusingly, referred to as a "cycle," with the current episode denoted as "cycle 24." Properties of each cycle such as duration, amplitude, and shape are measured and found to vary. We wish to similarly decompose the ∼12 year periodic signal of HD 30495 into individual cycles and measure their properties. For the Sun, this decomposition is typically done by identifying cycle minima in a smoothed time series of a proxy such as sunspot number, e.g., the 13-month boxcar smoothing of the monthly averages, and then using the minima as delimiters for each cycle (Hathaway 2010). The seasonal gaps in stellar time series do not allow us to use this same prescription. Instead, we construct an idealized smoothed model of the time series as a superposition of low-frequency sine waves:

$$S(t)_i = A_i \sin\left(\frac{2\pi}{P_i}(t + \phi_i)\right) + y_i \quad (2)$$

where P_i is a low-frequency period from a periodogram analysis, and the amplitude A_i, phase ϕ_i and offset y_i are found using a least squares optimization of this model to the mean-subtracted data. The final model is simply:

$$S(t) = \sum_i^{N_P} S(t)_i + \overline{S} \quad (3)$$

where N_P is the number of component sine waves and $\overline{S}$ is the original mean *S*-index.

We obtain the parameters of Equation (2) by iteratively finding the lowest-frequency period in a Lomb–Scargle periodogram of the composite *S*-index time series, fitting the sine to the data using a least-squares optimization, and subtracting the result from the data before computing the next periodogram. We carry out three such iterations in order to find

Table 2
HD 30495 Cycle Properties

Cycle	Start	Max	Duration	S_{max}	A_{cyc}
0	(1961.7)	1969.0	(15.3)	0.324	0.156
1	1977.1	1981.2	9.6	0.297	0.067
2	1986.7	1993.7	11.7	0.305	0.095
3	1998.4	2005.8	15.5	0.324	0.156
4	2013.9	…	…	…	…

the three low-frequency components revealed by the periodogram of the original dataset. The resulting model is akin to the result of a low-pass filter on the data. Indeed, subtracting the model from the data and computing the periodogram reveals that we have effectively removed most of the low-frequency power, as can be seen in Figure 4. The parameter set obtained from the fits of Equation (2) were $P = \{37.6, 18.8, 12.2\}$, $A = \{11.4, 4.68, 6.64\} \times 10^{-3}$, $\phi = \{-0.103, 5.93, 5.45\}$, and $y = \{-2.47, -0.0519, 1.26\} \times 10^{-3}$.

Using this model we characterized the individual cycles of HD 30495 as shown in Table 2. Quantities in parenthesis are based on an extrapolation beyond the data, and should be treated with caution. We see a spread in cycle durations from 9.6 to 15.5 year, with a mean value of the fully observed cycles 1–3 of 12.2 year. This value is close to the $P_{long} = 12.77$ year peak in the periodogram of Figure 3(b). We shall adopt the mean value of 12.2 year as our best estimate for the mean cycle period for HD 30495. The spread of individual cycle durations from the model gives us an estimate of the variability of cycle durations, $\Delta P_{long}/2 = 3.0$ year. The increase in cycle duration from cycle 1 to 3 obtained from our model agrees with the trend observed in the periodograms, with the earlier MWO series which includes cycles 1 and 2 having $P_{long,MWO} = 10.7$, and the later SSS series which only includes cycle 3 having $P_{long,SSS} = 15.3$ (see Figure 3(a)). The cycle model components at $P = 37.6$ and 18.8 year are artifacts of the amplitude structure in the time series and the data window, as discussed above. These components are necessary, however, to reconstruct the amplitude and cycle duration variability present in the original time series. For example, the amplitude $A = 6.64 \times 10^{-3}$ from the $P = 12.2$ year least-squares fit to the original data is not representative of the amplitude of the individual cycles seen in Figure 1(a), being at least a factor 2 too low. Only when the other two low-frequency components are included does the model amplitude more closely match the data.

The relative cycle amplitudes from the model are shown in column 6 of Table 2, defined as $A_{cyc} = \Delta S/\overline{S}$ following Soon et al. (1994) and Saar & Brandenburg (2002) studies of cycle amplitudes from the Mount Wilson program. Determining $\Delta S = S_{max} - S_{ref}$ requires us to select a reference point that approximates the lowest possible activity level for this star. Our cycle model does not effectively model the depth of the minima, as can be seen in Figure 1(a), which precludes its use for setting S_{ref}. Instead, we choose S_{ref} to be the lowest seasonal median with more than 3 measurements, $S_{ref} = 0.2763$ from the 1986 to 1987 season. This definition of activity minimum avoids too much sensitivity to outliers, while being low enough that only 3.6% of the data lie below this point. With our choice of S_{ref} and $\overline{S} = 0.303$ we find A_{cyc} ranging from 0.067 to 0.156, and a mean amplitude $\overline{A_{cyc}} = 0.118$. We find an increase in cycle amplitude from cycles 1 to 3, which occurs in parallel with the increase in cycle duration. Note that for the Sun the amplitude of a subsequent cycle is negatively correlated with cycle period (Hathaway 2010). The two transitions of fully observed cycles for HD 30495 indicate a positive correlation, though obviously no firm conclusions can be drawn from so little data.

Robustness of the cycle model was examined by running Monte Carlo simulations with the nightly measurements resampled from within their estimated uncertainties for each trial, then repeating the iterative procedure described above to compute the cycle model periods, amplitudes, phases, and offsets. The resulting minima positions, maxima positions, and amplitudes were gathered and the standard deviation of those distributions computed. The times of minima and maxima were found to be relatively robust forming a Gaussian distribution with a standard deviation of $\sigma = 0.25$ year. The amplitudes were also fairly robust, forming a Gaussian distribution with $\sigma = 8.6 \times 10^{-4}$. We use this to estimate the uncertainty in ΔS to be about 7%, which dominates the uncertainty of our relative amplitudes $A_{cyc} = \Delta S/\overline{S}$.

4. SHORT-PERIOD TIME-FREQUENCY ANALYSIS

A sine fit with $P = 1.58$ was found for the combined time series for a 5-year window centered at 2010.0 is shown in Figure 1(b), with the curve colored cyan within the fitting window and colored gray outside of the window. Comparing this sine wave to the data visually demonstrates the short-period variation, especially visible during the epoch of SMARTS measurements (cyan points). Even in this short segment we notice that the data goes out-of-step with the sine curve after 2012. This shows by example the quasi-periodic nature of the short-period variations, which was also evident in the triplet of peaks near $P \approx 1.6$ year in Figure 3(b).

To investigate possible coupling between the short- and long-period variations found above, we performed a periodogram analysis on a 5-year moving window of our combined S-index time series, the results of which are shown in Figure 5. First, we removed the low-frequency components from the data by subtracting the cycle model described in Section 3. Comparing Figure 4 panels (a) and (d), we see that this procedure amplifies the high-frequency peaks in the residual periodogram. However, we found the results of this analysis are qualitatively the same when working with the original composite time series. Next, the residual time series is divided into 1 year bins, which contain the entirety of the MWO/SSS seasonal observations. Every set of five consecutive bins are then subjected to a Lomb–Scargle periodogram analysis as described in Section 2, searching for periods from 1.1 to 2.5 years. Five-year windows were chosen as a sufficient time period to capture multiple oscillations of the $P \approx 1.6$ year variability detected in Figure 3(b). The period search cutoff at 1.1 year is to avoid aliasing issues related to the seasonal sampling, and the 2.5 year cutoff is to avoid strong signals associated with the duration of the window. In total, 44 periodograms were calculated as well as a 0.001 (99.9% significance) FAP threshold based on a Monte Carlo analysis as described in Section 2. Up to two significant peaks were extracted from these periodograms, and a least-squares fit of a sine function to the data window is done to determine the amplitude of that signal. In Figure 5 the normalized periodogram power is plotted as a contour area plot in the time-period plane, and the positions of significant peaks are plotted as open

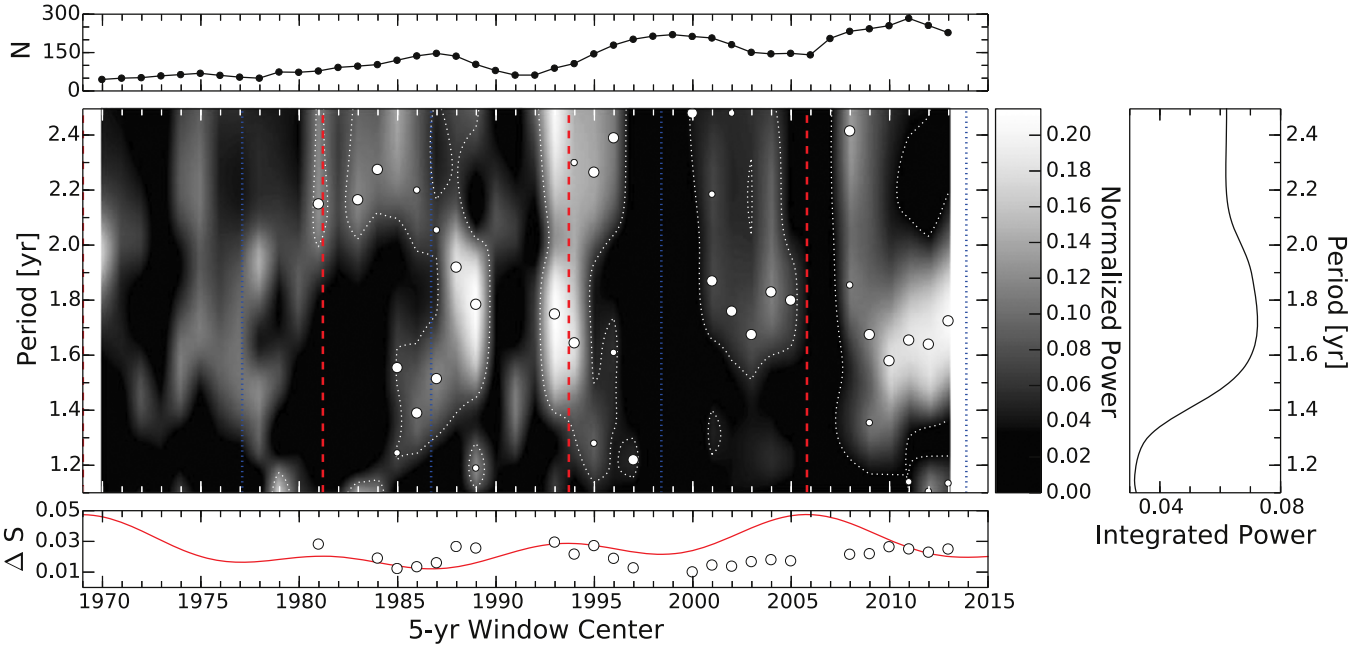

Figure 5. Short-time Lomb–Scargle analysis. A Lomb–Scargle periodogram is computed for 5 year moving windows in 1 year increments of the composite S-index time series for HD 30495. The contour plot gives the periodogram power normalized by the number of data points as a function of time and period, with the 99.9% significance contour highlighted as a dotted white line. The indicated time is for the center of the 5-year window. In each window, the highest peak above the 99.9% threshold is found and plotted as a large open circle, while a secondary significant peak, if present, is plotted as a small open circle. Vertical blue and red dashed lines indicate the minima and maxima in the long-term cycle model.The top panel indicates the number of data points in each 5-year window. The right panel gives the integrated normalized power for all windows. The bottom panel plots the amplitude ΔS of sine fits of the significant peak periods in the windowed data as open circles, with the amplitude of the three-component cycle model in red.

data points. The 99.9% significance contour is plotted as a dotted white line.

It is important to note that higher periodogram power is possible in time series with a larger number of data points, so that periodogram power does not scale equally from one window to the next. To check this behavior, we generated unevenly sampled time series of a sine function by randomly removing 50% of the data points and calculated the Lomb–Scargle periodogram, finding that periodogram power is proportional to the number of data points. To correct for this, we normalized the periodogram power by the number of data points in the window. Differences in periodogram power between windows are then due to differences in amplitude of the underlying signal. The number of data points in each window is plotted in the top panel of Figure 5 for reference. The 99.9% significance threshold is computed separately for each window, so the contour position is correct despite the difference in the number of data points.

Figure 5 reveals that variability near $P_{\rm short} \approx 1.6$ year is intermittent with peak periods occuring across the full range of periods analyzed. Significant peak variability in the 1.4–1.8 year range begins in 5-year windows centered at 1985, 1993, 2000, and 2009, with each episode lasting for 3–5 years. The 1985 and 2009 episodes precede the cycle 2 and 4 minima in the long-period cycle, respectively, while the 1993 and 2002 episodes roughly coincide with cycle maxima. In contrast to the minima of cycles 2 and 4, the cycle 1 and 3 minima are devoid of short period variability. Peaks are often found from ∼2.2 to ∼2.4 year as well, which is confirmed in the plot of the power integrated over all windows. Here the broad peak at ∼1.7 year is notably shifted from the cluster of narrow peaks in the periodogram of Figure 3(b). This may be due to varying phase in intermittent short-period signals leading to interference effects in the full-time-series periodogram. We will take the mean of the detected peak periods <2.0 year as our best estimate of the short-period signal, $P_{\rm short} = 1.67 \pm [0.35]$, where the quantity in brackets is half the observed range of peak periods.

We analyzed the peak-to-peak amplitudes ΔS of sine fits to the data with the significant peak periods in the range of 1.1 to 2.0 year and found them to range from 0.012 to 0.030, with a mean of 0.020. The average short-period relative amplitude $A_{\rm short} = \Delta S/\overline{S}$ is then $0.066 \pm [0.028]$, roughly half of the average long-period amplitude but nearly equal to relatively low amplitude of cycle 1, as deduced from our cycle model. We performed a rank-correlation test between the short-period amplitudes and the long-period cycle model, but no significant correlation was found.

From the above observations we conclude that there is no clear association between the long-period cycle and the episodic short-period variations. The presence or absence of the short-period variations are found in all phases of the long-term cycle, and the amplitudes are not correlated with the long-term cycle amplitude.

5. ROTATION

We repeated the rotation measurements done for six seasons of APT photometry in Gaidos et al. (2000) using the current 22-season record. The dense sampling of the APT program allows the detection of rotational modulations due to the transit of spots on the stellar photosphere. The time series is broken into individual seasons containing 55–185 measurements over the course of 150–200 days. From each season's time series a Lomb–Scargle periodogram was computed looking for rotational periods from 2 to 25 days. Peaks passing the 99.9%

significance level are taken as a signal of rotation. Uncertainty in the peak position was calculated using the Monte Carlo method described in Section 2 and ranged from 0.014 to 0.2 days. In total, rotational periods were detected in 17 of 22 seasons. Taking the mean, we find the average $P_{\rm rot} = 11.36 \pm 0.17$ days. This result is within the uncertainty of the previous Gaidos et al. (2000) measurement, as well as that of Baliunas et al. (1996) who obtained rotation from a densly sampled season of MWO S-index observations. The range of the precisely determined rotations are from 10.970 ± 0.028 to 11.560 ± 0.023 days, giving $\Delta P = 0.59 \pm 0.05$ day. This is reduced from the Gaidos et al. (2000) value of $\Delta P = 1.0$ days, due to the fact that we could not reproduce a significant 10.5 days detection in season 6. ΔP is interpreted as a sign of surface differential rotation, due to transiting spots at various latitudes. Our measurements range over one and a half stellar cycles, which increases the confidence that we have explored the full range of rotational periods which can be sampled with this technique. However, due to the unknown latitude ranges of the spots on the star, the measurement provides only a lower bound on the true equator-to-pole surface differential rotation.

The time series of rotation measurements and the seasonal activity-rotation relationship are shown in Figure 6. $P_{\rm rot}$ versus S is a kind of pseudo-butterfly diagram in the absence of spot latitude information, which would demonstrate different morphologies under different migration patterns (Donahue 1996). For example, in the Sun, if rotation were measured by tracking spots during the cycle we would expect a long rotation period and low activity at solar minimum (high latitude spots), transitioning to shorter rotation periods and higher activity until solar maximum (mid-latitude spots), and finishing with still shorter rotation periods as activity wanes (near-equator spots). A variety of morphologies were observed in Donahue (1996), including the anti-solar case. From Figure 6, we see that for HD 30495 in general rotation is slow when activity is high (with the exception of the 2008 season), but when activity is low both long and short rotation periods are seen. Tracing points in chronological order reveals no clear pattern, with seasons transitioning from quadrant to quadrant in the diagram. Near the maxima of cycle 3 ($t = 2005.8$, ref Table 2) there is a cluster of four seasons with slow rotation, 2004–2007. The 1997–1998 rotation was also slow, which occurred just before the minima at the start of cycle 3 ($t = 1998.4$), however the 2011 and 2013 rotation before the start of cycle 4 ($t = 2013.9$) was relatively fast. The lack of coherent structure in Figure 6 may be an indication that large spots which make the detection of $P_{\rm rot}$ possible are not restricted to a narrow range of latitudes as for the Sun.

Line of sight inclination is an important factor for interpreting the stellar rotation and activity data. We estimated the inclination using the $v \sin i$ measurement of Gaidos et al. (2000), together with $v = 2\pi R/P_{\rm rot}$, where R was derived using $g \propto M/R^2$ and the mass and surface gravity estimates of Baumann et al. (2010) (see Table 1), as well as our rotation measurement. We obtained $\sin i = 1.0 \pm 0.2$, indicating an equator-on view of the star, but the large uncertainty giving a one-sigma range of $i \gtrsim 55.^{\circ}4$. This perspective provides a best-case scenario for measuring rotation with spot transits, as well as a "solar-like" view of the activity cycles.

Finally, using the age–rotation relationship given in Equation (3) of Barnes (2007) along with our mean rotation period, we obtain an age of 970 ± 120 Myr. This revises the $t_{\rm gyro}$ from Table 3 of that work, which was based on a lower estimate for the rotation period.

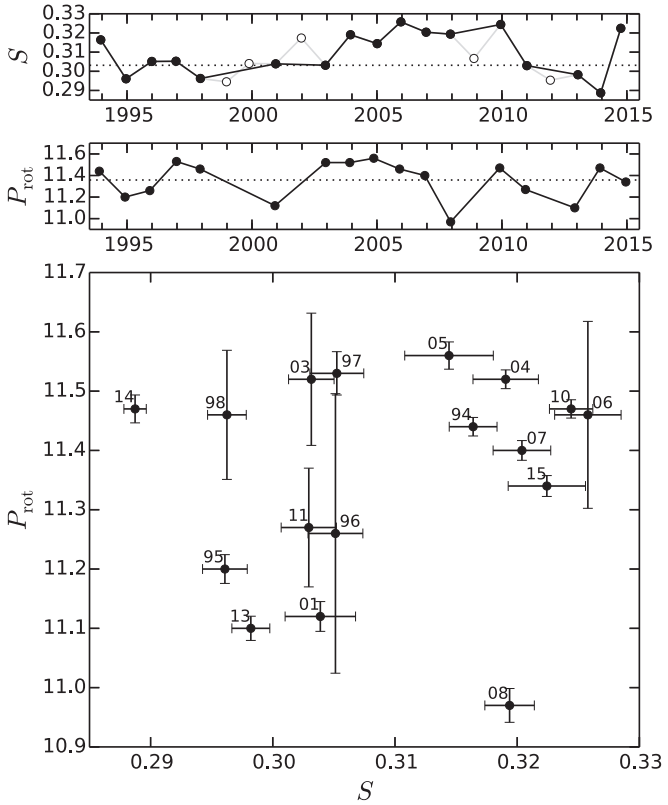

Figure 6. Top two panels: time series of seasonal rotation period measurements beneath seasonal mean S-index time series, for comparison. Filled (open) circles are measurements for seasons in which a rotation period detection was successful (unsuccessful). A horizontal dotted line marks the grand mean for the whole time series. Bottom panel: seasonal activity-rotation correlation plot, with error bars representing 1σ uncertainty in the rotation period and seasonal mean S value. Data points are annotated with the two-digit year.

6. DISCUSSION

We have observed quasi-periodic signals with representative values of $P_{\rm long} = 12.2 \pm [3.0]$ year and $P_{\rm short} = 1.67 \pm [0.35]$ year in the chromospheric activity of the fast-rotating ($P_{\rm rot} = 11.36 \pm 0.17$ days) solar analog HD 30495. A simple three-component sine cycle model shows three full cycles in the time series, each with varying duration and amplitude. This, combined with the improved signal-to-noise from our longer time series, has allowed us to demonstrate the "pronounced periodicity" that was previously lacking to classify this star as cycling in the Baliunas et al. (1995) study.

Taking the ratio of these periodicities to the rotation period, $n = P_{\rm cyc}/P_{\rm rot}$, we find $n_{\rm long} \approx 400\,{\rm rot/cyc}$ and $n_{\rm short} \approx 50\,{\rm rot/cyc}$, respectively, which closely correspond to the "active" and "inactive" sequences found in the stellar sample of Böhm-Vitense (2007). What is remarkable from that work is that the Sun appeared to be a unique outlier in that sample, with $n_{{\rm long},\odot} \approx 150$, and taking the solar QBO period as 2 years, $n_{{\rm short},\odot} \approx 30$. Why does the Sun appear as an outlier with respect to the stars? One explanation could be that the relatively small sample of 21 stars in Böhm-Vitense (2007) is insufficient to show the full picture of the relation between $P_{\rm cyc}$ and $P_{\rm rot}$, and further data will simply erase the observed trends. Indeed, the

sample of Saar & Brandenburg (1999), which is a superset of the Bohm-Vitense sample, includes a few neighboring points for the Sun on log plots of quantities proportional to $P_{\rm cyc}$ and $P_{\rm rot}$. Our datum for HD 30495, however, is decidedly not a neighbor of the Sun on these plots, while it agrees well with the trend set by stars on the active branch. Both the Sun and this star have a similar time scale for the observed long and short periodicities, yet rotation, $\overline{\Omega}_\star/\overline{\Omega}_\odot \approx 2.3$, is very different. This poses a serious problem for Babcock–Leighton flux transport dynamo models whose time scale is determined by the meridional flow. 3D hydrodynamic models show that meridional flow speed decreases with increased rotation rate (Ballot et al. 2007; Brown et al. 2008), but kinematic mean-field dynamos with one meridional flow cell have cycle times proportional to the flow speed and hence slower cycles with faster rotation. Jouve et al. (2010) investigated this problem, finding that multiple meridional flow cells in latitude were needed to make cycle period proportional to rotation. Unfortunately, observations to determine whether this indeed occurs in fast-rotating stars such as HD 30495 are nearly beyond imagination due to the extremely slow flow speeds, of order $\sim$10 m s^{-1} on the Sun.

We also compared relative amplitudes $A_{\rm cyc} = \Delta S/\overline{S}$ of the long and short variations to the stellar ensemble in Saar & Brandenburg (2002). We found the *average* cycle amplitude to be lower than the lowest star in that sample, though not excessively far from other active-branch stars, while the *maximum* amplitude (cycle 3) matches closely with the other active branch stars of similar $B - V$ color. That the average value is low is likely due to differences in methods used by Saar & Brandenburg (2002) (and Soon et al. 1994, the origin of part of the sample) which estimated peak-to-peak amplitude using the entire 25-year time series of the MWO sample. In addition, our method used the three-component cycle model and a global minimum defined by the lowest seasonal median in the time series, which by design filters out the variance from high-frequency components, resulting in a lower estimate in amplitude.

HD 30495 is nearly rotation and cycle-degenerate with the K2 star ϵ Eridani, which has $P_{\rm rot} = 11.1$ days and $P_{\rm long} = 12.7$ year, but a longer $P_{\rm short} = 2.95$ year (Metcalfe et al. 2013). In this comparison, the experimental variables include the depth of the convection zone, with stellar structure models predicting a deeper convective region for the cooler K star, as well as the average convective velocity. Apparently, these factors alone are not enough to prescribe a substantially different long-term cycle period.

In most dynamo theories, differential rotation is the driving force of the Ω-effect, responsible for turning poloidal magnetic flux into toroidal flux (e.g., Babcock 1961). Stars with greater differential rotation would be expected to "wind up" the field faster, and we should reasonably expect a shorter cycle time, as at least half of the process would be faster (the other half being the return of toroidal field to poloidal). Using our range of rotation period detections, the total measured surface rotational shear is $\Delta\Omega = 1\overset{\circ}{.}67 \pm 0\overset{\circ}{.}15$ day^{-1}. Then, using the the solar surface differential rotation result of Snodgrass & Ulrich (1990), we calculate the equator-to-pole total shear for comparison, finding $\Delta\Omega_\star/\Delta\Omega_\odot \geqslant 0.40 \pm 0.03$, which is a lower bound due to the unknown latitude ranges causing the rotation signal on the star. However, if one is prepared to assume that the spot latitudes of HD 30495 never form above 45°, as for the Sun, then differential rotation can be compared in terms of the solar shear from the equator to 45°, giving $\Delta\Omega_\star/\Delta\Omega_{45,\odot} \geqslant 1.02 \pm 0.09$. Both results allow the possibility that HD 30495 and the Sun have equivalent surface differential rotation, which might help to explain their similar cycle characteristics. Asteroseismic measurements of HD 30495 may be able to put tighter limits on $\Delta\Omega$ (Gizon & Solanki 2004; Lund et al. 2014).

Our time-frequency analysis does not indicate coupling between the intermittent short-period variability and the long-period cycle for this star. This is in contrast to the solar QBO, whose amplitude is strongly modulated by the 11 year cycle (Bazilevskaya et al. 2014). For HD 30495, the amplitudes of the short-period variations are at times larger than the amplitude of the long-term cycle, bringing into question which component of the variability is more fundamental to its dynamo. The absence of correlation between the two periodicities may be an indication that they are of a fundamentally different nature. It would be interesting to know at what time scale global magnetic field polarity reverses in this star, if indeed it does reverse. The S time series during the densely sampled SMARTS era shows a convincing sinusoidal variation, perhaps as convincing as the long-term trend. A campaign of Zeeman Doppler Imaging measurements spaced over at least a four year period should be able to determine if the short-period variability is polarity-reversing as well.

To the best of our knowledge, this is the first work to separate and characterize the amplitudes and durations of individual cycles from a stellar activity proxy. There are rich opportunities in this direction to explore the variability *of the cycles themselves*, as well as differences in stellar behavior during times of minima and maxima, which in turn can provide additional constraints for dynamo models. Already, the periodic signals measured here, together with the global properties collected in Table 1, present a well-characterized object to study with dynamo models. The existence of two significant time scales of variability in activity poses an additional modeling constraint. This bright object is also a prime candidate for future asteroseismic observations, which can further constrain its mass, radius, rotation profile, and depth of the convection zone (Metcalfe et al. 2009). Successful modeling of such well-described targets will hopefully lead to improved understanding of the dynamo process.

We are thankful to Willie Soon and Sallie Baliunas for providing data from the Mount Wilson survey. Thanks also to Jorge Melendez, Fabricio Freitas, and Megan Bedell for providing measurements derived from the HARPS spectrograph (program ID 188.C-0265). The authors thank Lou Boyd, Director of Fairborn Observatory, for his tireless efforts in support of our automated telescopes. Thanks to Piet Martens and Phil Judge for the useful discussions. We also thank the anonymous reviewer for their thoughtful comments, which led to substantial improvements in this manuscript. This research has made use of the SIMBAD database, operated at CDS, Strasbourg, France. This research also made use of Astropy, a community-developed core Python package for astronomy (http://astropy.org). R.E. is supported by the Newkirk Fellowship at the High Altitude Observatory. T.S.M. was partially supported by the Stellar Astrophysics Centre, which is funded by the Danish National Research Foundation under grant DNRF106. G.W.H. acknowledges support from NASA, NSF, Tennessee State University, and the State of Tennessee through its Centers of Excellence program.

APPENDIX
OBSERVATIONS

The observational data used in this study are available in the online version of this publication. Table 3 shows a sample of the nightly S measurements available from MWO, SSS, SMARTS, CPS, and HARPS shown in Figures 1(a) and (b). Note that the equal-mean calibration described in Section 2 is applied to these data; the data can be returned to its original calibration by dividing by the constants described there. Table 4 gives a sample of the nightly differential photometry measurements in the Strömgren b and y bands. Letting c_i be the ith column of Table 4, the $\Delta(b+y)/2$ time series of HD 30495 in Figure 2(c) is obtained using:

$$\Delta(b+y)/2_{\rm HD\ 30495} = \frac{1}{2}\left(\frac{c_2+c_4}{2}+\frac{c_3+c_5}{2}\right)$$

and subtracting the mean. The difference between the comparison stars is given by:

$$\Delta(b+y)/2_{\rm comps} = \frac{c_6+c_7}{2}.$$

The seasonal means of this series are shown as white squares in Figure 1(c). Finally, the color difference series $\Delta(b-y)$ of Figure 1(d) is given by:

$$\Delta(b-y)_{\rm HD\ 30495} = \frac{c_2+c_4}{2}-\frac{c_3+c_5}{2}.$$

Table 3
S-index Observations of HD 30495

(HJD–2,400,000)	S	σ_S	Instrument
41946.486	0.29000	0.00897	MWO
41960.475	0.31270	0.00897	MWO
41961.498	0.30230	0.00897	MWO
41962.484	0.30370	0.00897	MWO
42016.505	0.32040	0.00897	MWO

(This table is available in its entirety in machine-readable form.)

Table 4
Photometric Observations of HD 30495

Date (HJD–2,400,000)	$(P-C1)_b$ (mag)	$(P-C1)_y$ (mag)	$(P-C2)_b$ (mag)	$(P-C2)_y$ (mag)	$(C2-C1)_b$ (mag)	$(C2-C1)_y$ (mag)
49239.9956	−.4011	−.2222	−.2232	−.2816	−.1779	.0593
49248.9742	−.3969	−.2197	−.2234	−.2805	−.1734	.0607
49249.9655	−.4028	−.2237	−.2245	−.2825	−.1783	.0588
49250.9688	−.3988	−.2209	−.2230	−.2768	−.1758	.0559
49251.9645	−.3909	−.2144	−.2166	−.2708	−.1743	.0564
49252.9611	−.3925	−.2177	−.2175	−.2736	−.1749	.0558

(This table is available in its entirety in machine-readable form.)

REFERENCES

Babcock, H. W. 1961, ApJ, 133, 572
Baliunas, S., Sokoloff, D., & Soon, W. 1996, ApJL, 457, L99
Baliunas, S. L., Donahue, R. A., Soon, W. H., et al. 1995, ApJ, 438, 269
Ballot, J., Brun, A. S., & Turck-Chièze, S. 2007, ApJ, 669, 1190
Barnes, S. A. 2007, ApJ, 669, 1167
Baumann, P., Ramírez, I., Meléndez, J., Asplund, M., & Lind, K. 2010, A&A, 519, A87
Bazilevskaya, G., Broomhall, A.-M., Elsworth, Y., & Nakariakov, V. M. 2014, SSRv, 186, 359
Bedell, M., Meléndez, J., Bean, J., et al. 2015, A&A, 581, A34
Böhm-Vitense, E. 2007, ApJ, 657, 486
Brown, B. P., Browning, M. K., Brun, A. S., Miesch, M. S., & Toomre, J. 2008, ApJ, 689, 1354
Cayrel de Strobel, G. 1996, A&ARv, 7, 243
Chowdhury, P., Khan, M., & Ray, P. C. 2009, MNRAS, 392, 1159
Donahue, R. A. 1996, ApJ, 466, 384
Fares, R., Donati, J.-F., Moutou, C., et al. 2009, MNRAS, 398, 1383
Fletcher, S. T., Broomhall, A.-M., Salabert, D., et al. 2010, ApJL, 718, L19
Gaidos, E. J., Henry, G. W., & Henry, S. M. 2000, AJ, 120, 1006
Gizon, L., & Solanki, S. K. 2004, SoPh, 220, 169
Gray, R. O., Corbally, C. J., Garrison, R. F., et al. 2006, AJ, 132, 161
Habing, H. J., Dominik, C., Jourdain de Muizon, M., et al. 2001, A&A, 365, 545
Hall, J. C., Henry, G. W., Lockwood, G. W., Skiff, B. A., & Saar, S. H. 2009, AJ, 138, 312
Hall, J. C., & Lockwood, G. W. 1995, ApJ, 438, 404
Hall, J. C., Lockwood, G. W., & Skiff, B. A. 2007, AJ, 133, 862
Hathaway, D. H. 2010, LRSP, 7, 1
Henry, G. W. 1999, PASP, 111, 845
Horne, J. H., & Baliunas, S. L. 1986, ApJ, 302, 757
Howe, R., Christensen-Dalsgaard, J., Hill, F., et al. 2000, Sci, 287, 2456
Isaacson, H., & Fischer, D. 2010, ApJ, 725, 875
Jouve, L., Brown, B. P., & Brun, A. S. 2010, A&A, 509, A32
Liseau, R. 1999, A&A, 348, 133
Lovis, C., Dumusque, X., Santos, N. C., et al. 2011, A&A, submitted (arXiv:1107.5325)
Lund, M. N., Miesch, M. S., & Christensen-Dalsgaard, J. 2014, ApJ, 790, 121
McIntosh, S. W., Leamon, R. J., Krista, L. D., et al. 2015, NatCo, 6, 6491
Metcalfe, T. S. 2009, in ASP Conf. Ser. 416, Solar-Stellar Dynamos as Revealed by Helio- and Asteroseismology: GONG 2008/SOHO 21, ed. M. Dikpati et al. (San Francisco, CA: ASP), 567
Metcalfe, T. S., Basu, S., Henry, T. J., et al. 2010, ApJL, 723, L213
Metcalfe, T. S., Buccino, A. P., Brown, B. P., et al. 2013, ApJL, 763, L26
Noyes, R. W., Hartmann, L. W., Baliunas, S. L., Duncan, D. K., & Vaughan, A. H. 1984, ApJ, 279, 763
Oláh, K., Kolláth, Z., Granzer, T., et al. 2009, A&A, 501, 703
Perryman, M. A. C., Lindegren, L., Kovalevsky, J., et al. 1997, A&A, 323, L49
Porto de Mello, G. F., da Silva, R., da Silva, L., & de Nader, R. V. 2014, A&A, 563, A52
Ramírez, I., Meléndez, J., Bean, J., et al. 2014, A&A, 572, A48
Saar, S. H., & Baliunas, S. L. 1992, in ASP Conf. Ser. 27, The Solar Cycle, ed. K. L. Harvey (San Francisco, CA: ASP), 150
Saar, S. H., & Brandenburg, A. 1999, ApJ, 524, 295
Saar, S. H., & Brandenburg, A. 2002, AN, 323, 357
Scargle, J. D. 1982, ApJ, 263, 835
Skumanich, A. 1972, ApJ, 171, 565
Snodgrass, H. B., & Ulrich, R. K. 1990, ApJ, 351, 309
Soon, W. H., Baliunas, S. L., & Zhang, Q. 1993, ApJL, 414, L33
Soon, W. H., Baliunas, S. L., & Zhang, Q. 1994, SoPh, 154, 385
van Leeuwen, F. 2007, A&A, 474, 653
Vaughan, A. H., Preston, G. W., & Wilson, O. C. 1978, PASP, 90, 267
Wilson, O. C. 1968, ApJ, 153, 221
Wilson, O. C. 1978, ApJ, 226, 379